Structural characterizations of organic-based materials with extensive mechanoluminescence properties

Structural characterizations of organic-based materials with extensive mechanoluminescence properties

[a]R.A.D.M. Ranashinghe, [b]Yasutaka Tanaka, [b]Masayuki Okuya, [b]Masaru Shimomura and

[b]Kenji Murakami

[a]*Graduate School of Science and Technology, Shizuoka University, Japan*

[b]*Graduate School of Integrated Science and Technology, Shizuoka University, Japan*

Corresponding author: E-mail: murakami.kenji@shizuoka.ac.jp

mobile: +818016191131

Keywords: structure, organic polymer-based mechanoluminescence, polyvinylpyrrolidone

Abstract: The organic mechanoluminescent (ML) material europium-doped dibenzoylmethide triethylammonium (EuD_4TEA) is known as a triboluminescent material. Our group has synthesized a novel ML material with the addition of 1-ethenylpyrrolidin-2-one [(polyvinylpyrrolidone) (PVP)], which changed the ligand of the mechanoluminescent material. This research investigated the ML material structure, molecular orbital electron distributions of the ligands, ML mechanism and enhancement in the photoluminescence (PL) intensity with PVP. For the first time, the ML material structure was characterized using nuclear magnetic resonance spectroscopy (NMR), X-ray diffraction (XRD), X-ray photoelectron spectroscopy (XPS) and Gaussian DFT/B3LYP/6-31G(d,p) software. The ML properties were characterized using a Hamamatsu Photonic Multichannel Analyzer (PMA). The material can be applied to the real-time

visualization of the stress field near the tip of a crack, an ML light source, determination of laser and ultrasonic powers, secret message writing and earthquake detection sensors.

1. Introduction

Mechanoluminescence (ML) is a light-emission event that results from a mechanical action on a solid[1]. Fracto-, plastico- and elastico-ML are various forms of ML. Among the various ML forms, fracto-ML is well known because most inorganic materials emit light when they fracture as a result of the plate force during and prior to an earthquake [2-4]. Additionally, plastico-ML can be observed by peeling an adhesive tape in a vacuum [5, 6]. When the crystal bonds are broken along oppositely charged planes and then reconnect, light is emitted as the charges pass through the gaps that were created from the fracture [7, 8]. Once the material is fractured, the electrons are excited to higher energy levels and then transition to the lower energy levels [9, 10]. The energy difference between the corresponding levels is emitted as a light with different wavelengths [11]. The third type of ML mechanism, elastico-ML, results from a mechanical stress that produces a piezoelectric field on the surface of crystals[12-14]. This electric field that is near the color center is high because of changes in the local structure. These changes may reduce the carrier trap depth or effect band bending [15-17]. After decreasing the carrier trap depth, the thermal de-trapping of the carriers may occur. Trapped charge carriers can tunnel to the conduction band because of the band bending. The electrons from the conduction band may be captured by the excited state of the activator ions. This may cause a de-excitation of the color center and produce the emission[18]. When plastico-mechanoluminescent materials are plastically deformed, a movement of dislocation occurs. Similarly, an electric field generated by the charge dislocation causes a bending of the valance, conduction and dislocation bands. Trapped electrons tunnel to the conduction band and

the recombination of electrons and holes enables the light emission characteristic of the color center. However, the conduction band electrons are trapped by the color center and a potential energy transfer occurs as a result of the de-excitation of the rare earth cation. Both functions occur and electron-hole recombination is greater than that caused by the impact excitation[19]. The mechanism of the fracto-ML material is believed to be different. In this case, when the material fractures, two newly created, oppositely charged surfaces are generated, which produce an electric field and cause a dielectric breakdown of the surrounding gasses and, in turn, may give rise to gaseous discharge ML. Additionally, the electric field that caused the dielectric breakdown of the crystals and the recombination of the free carriers may lead to recombination luminescence [20, 21]. To date, many inorganic mechanoluminescent materials have been synthesized with various dopants[22-24], such as Eu, dialuminum strontium oxygen(2-)$SrAl_2O_4$: Eu[25], Eu, Barium(2+), oxido(oxo)aluminum $BaAl_2O_4$: Eu[26], Eu, Dy, dialuminum strontium oxygen(2-)$SrAl_2O_4$: Eu, Dy[27] and zinc sulfide, ZnS: Mn[28]. However, the difficulty is that they are typically synthesized at high temperatures that are greater than 1000 °C[29].

Our study is focused on the structure of the synthesized material, the ML and the mechanism for the increase in PL intensity. We have determined the structure of this synthesized ML material using nuclear magnetic resonance spectroscopy (NMR), X-ray photoelectron spectroscopy (XPS) and the molecular orbital diagram of the ligands. This paper has reviewed the structure of the synthesized ML material, mechanism of the intensity enhancement and crystallinity of the ML material.

2. Experimental

The synthesis of the PVP-based dibenzoyl methide triethylammonium compound was based on the our previously reported procedures and methods [30].

First, 80 ml ethyl alcohol (99.9%, Wako) was heated to 70 °C and then 0.8 mmol 1, 3-diphenylpropane-1,3-dione (99%, Wako) (DBM) was added to the solution mixture and stirred. Next, the solute was completely dissolved and 0.3 mmol europium nitrate hexahydrate (99.9%, Wako) was added to the mixture. Then, 0.1 g PVP (99%, Wako) and 0.5 ml N,N-diethylethanamine, triethylamine (99.8%) (TEA) were added. After adding the compounds, the solution was maintained at 70 °C for 20 min. Then, the solution vessel was tightly capped and placed in a thermos overnight. The regulated slow cooling in the thermos was critical for optimal crystal formation. For comparison, a material that was based on EuD_4TEA without PVP was also synthesized. Photoluminescence (PL) and ML properties were measured for both of the synthesized materials at room temperature.

2.1 Characterization

The mechanoluminescence and photoluminescence intensities were characterized using a photonic multichannel analyzer. The absolute values of higher occupied molecular orbital (HOMO) and lower unoccupied molecular orbital (LUMO) energy levels of each chemical were characterized using Gaussian DFT/B3LYP/6-31G(d,p) software. Scanning electron microscopy (SEM), scanning transmission electron microscopy (STEM) and field emission scanning electron microscopy (FESEM) were conducted on a JEM-2100F electron microscope. X-ray diffraction (XRD) images were collected using a Rigaku RINT-Ultima III diffractometer. XPS measurements were performed using a KRATOS AXIS Ultra spectrometer.

3. Results and Discussion

3.1. Mechanoluminescence and photoluminescence study

Figure 1 shows an ML intensity comparison for specimens before and after the addition of the PVP polymer. These spectra clearly show an increase in the ML intensity after the addition of PVP. The solid curve corresponds to the ML enhancement of the material with a larger quantity of europium nitrate hexahydrate. However, europium nitrate hexahydrate with the addition of PVP resulted in a higher ML intensity (red curve). The PVP polymer bonded with $Eu^{+3}$and facilitated a higher electron-transition rate and hence a greater excitation. Additionally, the results suggest that the local environment surrounding the Eu^{+3} ion was more disordered. Hence, the degree of polarization for europium-doped dibenzoylmethide triethylammonium was higher when PVP was infused into the ML material. This led to a higher probability for electric dipole-allowed transitions. Figure 2 shows the spectra of the PL intensity of the formed ML material before and after the addition of the PVP polymer. The corresponding PL emission wavelengths are 592.7 nm, 612.0 nm, 651.2 nm and 701.3 nm. All the emission lines belong to the europium $^5D_0$ to ^7F_n (n=1, 2, 3 and 4) electron energy transitions. However, after PVP addition in the synthesized materials, the ML and PL emission intensities increased.

3.2. Crystallography and structural studies

Figures 3 and 4 show the X-ray diffraction patterns for EuD_4TEA without and with PVP, respectively. In Figure 3, the 2Θ values at 6.68, 6.87, 7.00 and 7.60 correspond to the (112), (120), (020) and (102) Millar planes, respectively, (JCPDS card number 96-711-8092). The crystal

structure matched the europium, 2,2′ -bipyridine 5,5′ -dicarboxylic acid compound and the crystal system was monoclinic. Figure 4 depicts that the XRD profile for the synthesized ML material with PVP and the 2Θ values at 6.88, 6.97, 7.53, 7.83 and 10.39 that correspond to the (020), (012), (102), (211) and (011) Millar planes, respectively, (JCPDS card number 96-711-8093). The crystal system was monoclinic and similar to europium,2,2′ -bipyridine 5,5′ -dicarboxylic-Cu. A comparison with the TEM micrograph in Figure 5(c) clearly shows that the structure has grown along the vertical c-axis and has a rod-like shape. Therefore, the monoclinic structure was confirmed. The mean value of the grain size in the synthesized materials before the addition of PVP was calculated to be approximately 7 nm using the de Debye Scherer equation. A comparison with the histograms in Figures 5(e) and 6(d) confirmed that the particle size was comparable to that revealed by the XRD calculation. After the addition of PVP, the TEM micrographs in Figure 6(a) and (b) clearly show an unchanged structure and an increase in the nanorod-shaped structures in the novel material. The TEM images depict fine ML particles and the corresponding histogram (Figure 6(d)) shows a mean value of 4 nm for the calculated particle size. A comparison with the XRD profiles of the calculated grain size showed similar results and also provided evidence for the crystallinity of the newly formed organic-based mechanoluminescent material. The low defect site concentration in the crystalline material resulted in better electron transport properties without trapping and recombination. The newly synthesized EuD_4TEA material with PVP has shown higher ML and PL intensities than without PVP. After the addition of PVP, the crystallinity of the ML material increased and the enhanced electron density of the unit cell caused a higher ML intensity.

Figure 5 shows TEM micrographs of the synthesized ML material without PVP and with fine particles. Image Figure 5(d) shows the small particles that correspond to a 7 nm size. Figure 5 (c)

reveals that the structure of the material exhibits a nanorod-like shape and the rod-like structure is integrated with the fine particles. However, a comparison with the histogram of the SEM micrograph in Figure 5(a) indicates that the average particle size was approximately 7 nm. In Figure 6, the TEM micrographs and corresponding histogram (Figure 6(d)) reveal that the particle sizes became finer after the addition of PVP and their average size was approximately 4 nm. Particle size analysis was performed using ImageJ software[31]. According to the TEM micrographs, the PVP molecules were attached to each crystal and these results were also confirmed by the XPS data. This molecular attachment caused an intensity enhancement because of the reduced electron back-transfer rate when the electron crossed the intersystem from the singlet excited state to the triplet energy state. The ML intensity depends on the critical distance of the ligand material, color center and electron's intersystem-crossing and back-transfer rates. Particle sizes of a few nanometers enable the convenient intersystem crossing of the electrons and may have caused the electrons to be captured by the color center. Because the distance between the ligand and color center was small, the electron orbital overlap increased. After adding PVP, the ML crystal size was approximately 4-5 nm and therefore there was in increase in intensity compared with the synthesized material without PVP. Figure 7 displays the ^{1}H NMR spectrum of the ML material without PVP. For the first time, an NMR analysis of the structure of the EuD_4TEA ML material was performed. The peaks at 1.17286 ppm and 2.7001 ppm correspond to the proton in the CH_3 and CH_2 groups, respectively. In Figure 6, the peaks at 11.4401 ppm and 46.40260 ppm correspond to ^{13}C in the CH_3 and CH_2 groups, respectively. The peaks between 7.24122 ppm and 8.15117 ppm in the ^{1}H spectrum and 127.00645 ppm and 132.59652 ppm in the ^{13}C spectrum revealed a dibenzoylmethane group. In Figure 8, the peaks from 76.57252 pm to 77.41926 ppm belong to Trichloro(^{2}H)methane ($CDCl_3$). However, we used TEA and DBM; therefore, the total

number of protons in TEA should be 15. Figure 9 revealed that the total number of protons that belong to the methyl and ethyl groups are approximately 14. Therefore, those peaks correspond to TEA. The total number of protons in the DBM molecule is 11 and ^{1}H proton NMR spectrum shows 30 protons that correspond to the DBM peak region. Therefore, 3 DBM molecules are represented and it is believed that smallest ratio between TEA and DBM to coordinate with Eu^{+3} is 1:3. However, if the color coordination number on Eu^{+3} ratio is considered, then the ratio can be 2:6.

3.3. Molecular orbital study

We performed theoretical calculations to analyze the electronic structures of triethylamine (TEA), polyvinylpyrrolidone (PVP) and dibenzoylmethane (DBM). Figures 10, 11 and 12 show the absolute value of the molecular orbitals (MOs), higher unoccupied molecular orbital (HOMO) and lower occupied molecular orbital (LUMO) images for PVP, TEA and DBM, respectively. In Figure 10, the MOs of DBM are localized near the phenyl groups and according to the DBM electron density mapping, the electron density surrounding the two oxygen atoms is higher. Figure 11 demonstrated that the HOMO and LUMO of PVP are localized near the pyrrole group and a higher density of electrons are localized around the N and O atoms. These molecular orbital diagrams exhibit the strong possibility that PVP and DBM will coordinate with the europium color center. Figure 12 revealed that the HOMO and LUMO levels of trimethylamine surround all the atoms and the electron density is localized near the N atom.

Figure 5(a) shows SEM images of the ML material without PVP and the micrographs clearly demonstrate that material has a rod-like structure. The TEM micrograph in Figure 5 (c) also confirms that the material exhibits a rod-like structure after the addition of PVP. However, the

homogeneity of the fine particles is uneven, and the particle size distribution that ranged from approximately 10 nm to 40 nm of particles distribution was increased. The material structure was larger compared with the structure of the ML material with PVP. This increase was caused by an electron transition through the material. When the particle size decreases, the molecular orbital overlap is increased. Therefore, the electron can easily transition to the higher and lower energy levels. It is believed that after the addition of PVP, the ML intensity was high. Additionally, the theory behind the mechanism of the mechanoluminescent material is unknown. The intensity of the ML material depends on the energy difference of the electron transition state. ML depends on the flexibility of the ligand molecule, which coordinates to the color center. Trimethylamine has a greater flexibility compared with the other inorganic molecules. When the ML material is under stress, the ligand molecule can easily move in all directions. Because of this movement, the molecular orbitals overlap and the electrons can transit to a higher energy level. However, the unsteady electrons fall to the lower energy levels. The energy difference between those energy states is illuminated as light. Eu^{+3}-coordinated polyvinylpyrrolidone molecules are highly flexible and therefore the intensity of the ML material significantly increased.

Figure 13 depicts the XPS spectra of the ML materials synthesized both before and after the addition of PVP. The spectra clearly show that both materials have C, O, N and Eu. In the C1s spectra, the two main peaks between binding energies of 280 eV and 285 eV correspond to the C in dibenzoylmethane. A component that was higher than 5 eV from the main peak in the C1s spectra was found without PVP. This peak was assigned to the C=O functional group and disappeared with the addition of PVP. This disappearance confirms the decrease in coordination of the dibenzoylmethane group after the addition of PVP into the ML material and is caused by a larger amount of PVP molecules attached to the color center. In both materials, a component that

is greater than 1 eV from the main peak was detected. This main peak can be assigned to a C-OH functional group, which can be attributed to water absorption on the synthesized ML material and to the intensity of that peak decreased with the addition of PVP. Furthermore, the PVP polymer material has a hydrophobic property, which caused a smaller amount of water absorption. There is not a significant difference in the Figure 14 Eu 4d spectra, but the peak area increased with the addition of PVP. The spectrum provides evidence that the Eu^{+3} valence is not changed with PVP. In Figure 15 the O1s spectra, a component that was higher than the main peak was found prior to the addition of PVP. This component was assigned to the C=O ∏ bond and disappeared after the addition of PVP. However, a higher number of molecules were coordinated with the Eu^{+3} color center with PVP. This highly intense new material can be used for various purposes, such as defect determination in pipes, stress sensor analyses, real-time visualization of the stress distribution in solids, internal visualization of artificial legs, real-time visualization of the quasidynamic crack-propagation in solids, novel ML-driven solar cell systems, real-time visualization of the stress field near the tip of a crack, ML light sources, determination of laser and ultrasonic powers, secret message writing, EML-based safety-management monitoring systems, non-destructive testing of materials, earthquake detectors and sensors for the detection of cracks inside concrete beams.

4. Conclusions

For the first time, we have investigated the minimum ratio between TEA and DBM (1:3) from an analysis of ^{1}H and ^{13}C NMR spectra. The XPS results indicate that the materials have peaks that correspond to C, O, N and Eu. The ML and PL intensities were characterized using a Hamamatsu photonic multichannel analyzer. The PL spectrum that was collected after a 357 nm excitation consisted of emission lines at 592.7 nm, 612.0 nm, 651.2 nm and 701.3 nm. Those emission wavelengths belong to an electron transition from the $^{5}D_0$ to $^{7}F_n$ (n=1, 2, 3, 4) energy levels. The corresponding XRD patterns provide evidence that the novel material has good crystallinity with PVP. The corresponding TEM images have confirmed that the material has a rod-like structure, and a histogram confirmed particle sizes at approximately 4 nm. The histogram from the TEM micrographs and XRD results of the material without PVP confirm a mean value of grain size from approximately 7 nm to 10 nm. After the addition of PVP, a decrease in the particle size was confirmed. The fine particle size and crystallinity of the synthesized ML material enabled a higher overlap in the electron orbitals. The greater electron orbital overlap, a flexibility of the ligand molecules and a higher dipole moment of PVP resulted in an increase in the ML and PL intensities of the synthesized ML material. The newly synthesized EuD_4TEA material with PVP has higher PL and ML intensities compared with the material without PVP. Because the novel material has a higher ML intensity, it can be applied to defect detection in pipes, stress sensor analyses, real- time visualization of the stress distribution in solids, internal visualization of artificial legs, real-time visualization of the quasidynamic crack-propagation in solids, novel ML-driven solar cell systems, and real-time visualization of the stress field near the tip of a crack and used as an ML light source.

5. Acknowledgments

This work was supported by the Department of Optoelectronics and Nanostructures' Science, Graduate School of Science and Technology, Shizuoka University, Japan.

6. Abbreviations

Triethylamine, dibenzoylmethane, $Eu(NO)_3.6H_2O$

7. References

[1. Tiwari, N., V. Dubey, and R.K. Kuraria, *Mechanoluminescence Study of Europium Doped CaZrO3 Phosphor.* Journal of Fluorescence, 2016. **26**(4): p. 1309-1315.
2. Chandra, B.P., *Mechanoluminescence*, in *Luminescence of Solids*, D.R. Vij, Editor. 1998, Springer US: Boston, MA. p. 361-389.
3. Jha, P. and B.P. Chandra, *Survey of the literature on mechanoluminescence from 1605 to 2013.* Luminescence, 2014. **29**(8): p. 977-993.
4. Chandra, B.P., et al., *Sensing of shock-wave velocity and pressure using shock-wave induced mechanoluminescence of crystals.* Sensors and Actuators A: Physical, 2015. **235**: p. 203-209.
5. Putterman, S.J., et al., *Mechanoluminescent x-ray generator*. 2014, Google Patents.
6. Teotonio, E.E.S., et al., *Mechanoluminescence of Coordination Compounds*, in *Triboluminescence: Theory, Synthesis, and Application*, O.D. Olawale, et al., Editors. 2016, Springer International Publishing: Cham. p. 39-63.
7. Reynolds, G.T. and R.H. Austin, *Mechanoluminescence of plastic scintillation counters.* Journal of Luminescence, 2000. **92**(1–2): p. 79-82.
8. Xu, C.N., et al., *Preparation and characteristics of highly triboluminescent ZnS film.* Materials Research Bulletin, 1999. **34**(10–11): p. 1491-1500.
9. Takada, N., et al., *Mechanoluminescence from piezoelectric crystals of an europium complex.* Synthetic Metals, 2000. **111–112**: p. 587-590.
10. Chandra, B.P., *Mechanoluminescence and high pressure photoluminescence of (Zn, Cd) S phosphors.* Pramana, 1982. **19**(5): p. 455-465.
11. Chandra, B.P., V.K. Chandra, and P. Jha, *Models for intrinsic and extrinsic fracto-mechanoluminescence of solids.* Journal of Luminescence, 2013. **135**: p. 139-153.

12. Chandra, B.P., V.K. Chandra, and P. Jha, *Microscopic theory of elastico-mechanoluminescent smart materials.* Applied Physics Letters, 2014. **104**(3): p. 031102.
13. Chandra, V.K. and B.P. Chandra, *Suitable materials for elastico mechanoluminescence-based stress sensors.* Optical Materials, 2011. **34**(1): p. 194-200.
14. Jeong, S.M., et al., *Mechanoluminescence Color Conversion by Spontaneous Fluorescent-Dye-Diffusion in Elastomeric Zinc Sulfide Composite.* Advanced Functional Materials, 2016. **26**(27): p. 4848-4858.
15. Botterman, J., et al., *Mechanoluminescence in BaSi2O2N2:Eu.* Acta Materialia, 2012. **60**(15): p. 5494-5500.
16. Chandra, B.P., et al., *Real-time mechanoluminescence sensing of the amplitude and duration of impact stress.* Sensors and Actuators A: Physical, 2012. **173**(1): p. 9-16.
17. Wang, X., et al., *Dynamic Pressure Mapping of Personalized Handwriting by a Flexible Sensor Matrix Based on the Mechanoluminescence Process.* Advanced Materials, 2015. **27**(14): p. 2324-2331.
18. Rahimi, M.R., et al., *Effects of persistent luminescence decay on mechanoluminescence phenomena of SrAl2O4:Eu2+, Dy3+ materials.* Optics Letters, 2013. **38**(20): p. 4134-4137.
19. Chandra, V.K., B.P. Chandra, and P. Jha, *Models for intrinsic and extrinsic elastico and plastico-mechanoluminescence of solids.* Journal of Luminescence, 2013. **138**: p. 267-280.
20. Chandra, B.P., et al., *Fracto-mechanoluminescence and mechanics of fracture of solids.* Journal of Luminescence, 2012. **132**(8): p. 2012-2022.
21. Li, D.G., N.S. McAlpine, and D. Haneman, *Surface barriers and potentials from luminescence on cleaved Si, GaAs, and InP.* Surface Science, 1993. **281**(1): p. L315-L320.
22. Lin, Y.-H., et al., *Studies on mechanoluminescence from SrAl2O4:Eu, Dy phosphor.* Materials Chemistry and Physics, 2003. **80**(1): p. 20-22.
23. Zhang, J.-C., et al., *Controlling elastico-mechanoluminescence in diphase (Ba,Ca)TiO3:Pr3+ by co-doping different rare earth ions.* RSC Advances, 2014. **4**(77): p. 40665-40675.
24. Chandra, B.P., et al., *Strong mechanoluminescence induced by elastic deformation of rare-earth-doped strontium aluminate phosphors.* Journal of Luminescence, 2009. **129**(7): p. 760-766.
25. Imai, Y., R. Momoda, and C.-N. Xu, *Elasticoluminescence of europium-doped strontium aluminate spherical particles dispersed in polymeric matrices.* Materials Letters, 2007. **61**(19–20): p. 4124-4127.
26. Kaur, J., et al., *Optical properties of rare earth-doped barium aluminate synthesized by different methods-A Review.* Research on Chemical Intermediates, 2015. **41**(4): p. 2317-2343.
27. Chandra, B.P., et al., *Mechanoluminescence glow curves of rare-earth doped strontium aluminate phosphors.* Optical Materials, 2011. **33**(3): p. 444-451.
28. Sharma, R., et al., *Mechanoluminescence and thermoluminescence of Mn doped ZnS nanocrystals.* Journal of Luminescence, 2011. **131**(10): p. 2089-2092.
29. Pust, P., et al., *Narrow-band red-emitting Sr[LiAl3N4]:Eu2+ as a next-generation LED-phosphor material.* Nat Mater, 2014. **13**(9): p. 891-896.

30. R, A.D.M.R., et al., *Effect of added polyvinylpyrrolidone on mechanoluminescent property of europium-doped dibenzoylmethide triethylammonium.* JJAP Conference Proceedings, 2016. **011105**: p. 4.
31. Schneider, C.A., W.S. Rasband, and K.W. Eliceiri, *NIH Image to ImageJ: 25 years of image analysis.* Nat Meth, 2012. **9**(7): p. 671-675.

Fig.1 Mechanoluminescent intensity spectra of europium tetrakis dibenzoylmethide triethylammonium synthesized with and without PVP.

Fig. 2 Comparison of the photoluminescence intensity spectra of the ML material with and without PVP.

Fig. 3 XRD pattern of the ML material without PVP.

Fig. 4 XRD pattern of the ML material with PVP.

Fig. 5 (a) FESEM, (b) histogram obtained by using FESEM micrograph, (c)/(d) TEM micrographs and (e) histogram correlated to TEM micrographs of the synthesized ML material without PVP.

Fig. 6 (a)/(b) TEM micrographs, (c) FESEM micrograph and (d) histogram correlated with TEM image (b) of the synthesized novel ML material with PVP.

Fig. 7 ^{1}H NMR spectrum of the ML material without PVP

Fig. 8 ^{13}C NMR spectrum of the ML material without PVP

Fig. 9 The crystal structure of the synthesized ML material that was illustrated using Avogadro 1.0.1software.

Fig. 10 MO contour plots of dibenzoylmethane that were calculated using DFT methods.

Fig. 11 MO contour plots of PVP that were calculated using DFT methods.

Fig.12 MO contour plots of the triethylamine that were calculated using DFT methods.

Fig. 13 Comparison of XPS spectra obtained from the synthesized materials before and after the addition of PVP.

Fig. 14 Comparison of Eu 4d spectra with and without PVP.

Fig. 15 Comparison of O1s spectra with and without PVP.

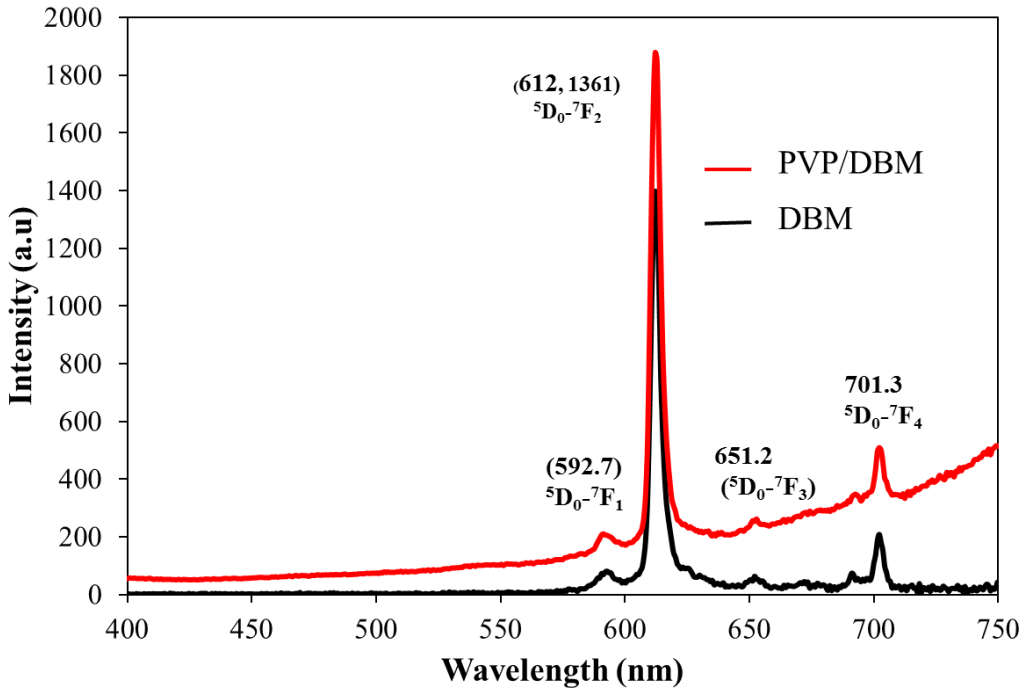

Figure 1

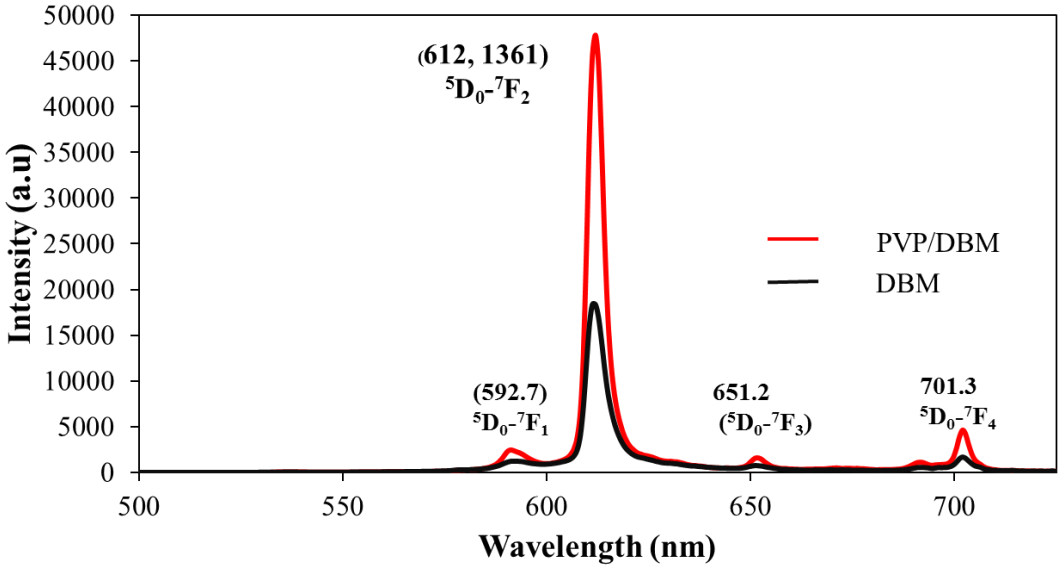

Figure 2

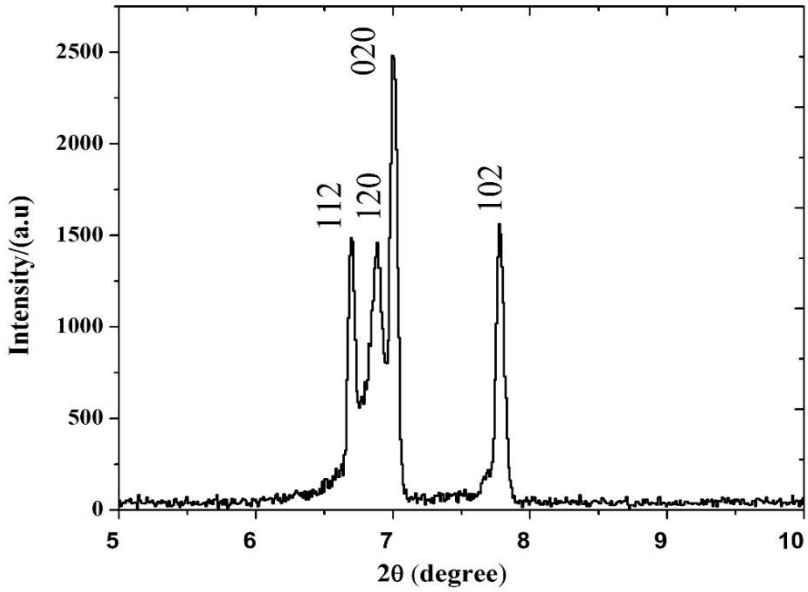
Intensity/(a.u)
2θ (degree)
112
120
020
102
0
500
1000
1500
2000
2500
5
6
7
8
9
10

Figure 3

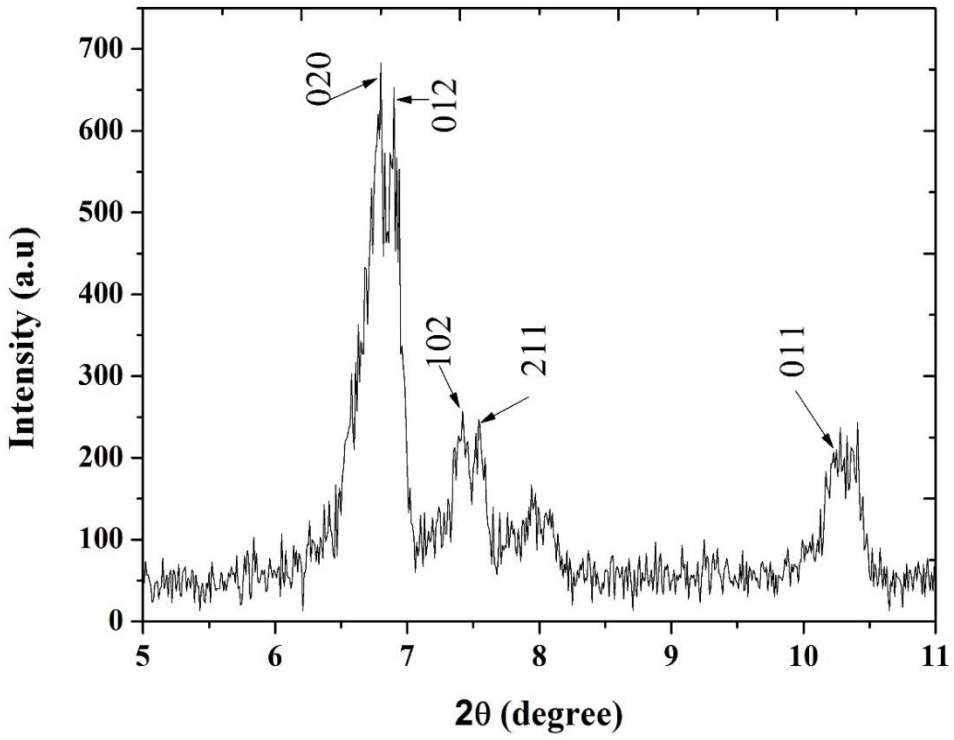
Intensity (a.u)
2θ (degree)
020
012
102
211
011
0
100
200
300
400
500
600
700
5
6
7
8
9
10
11

Figure 4

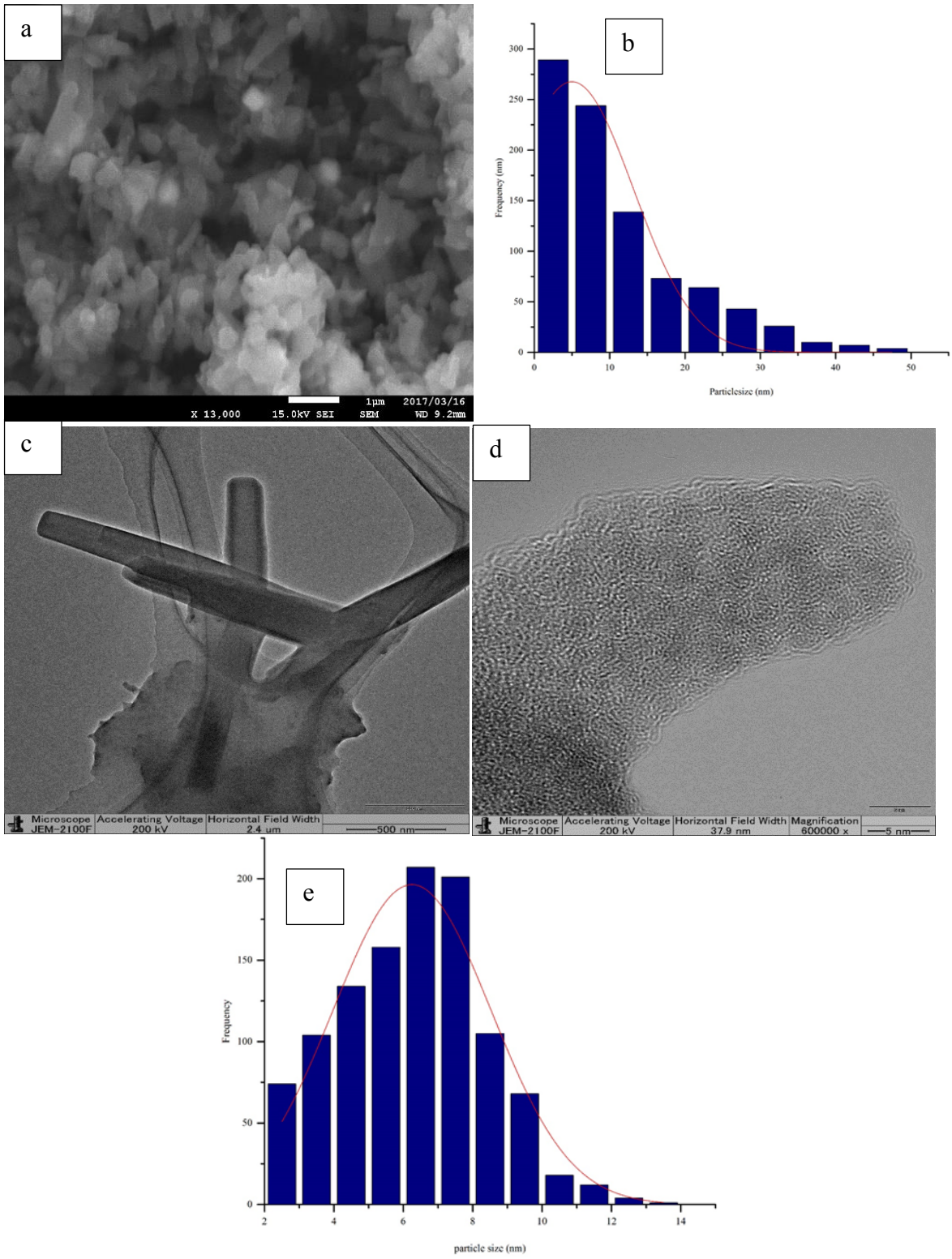
a
X 13,000 15.0kV SEI 1μm SEM 2017/03/16 WD 9.2mm
b
Frequency (nm)
Particlesize (nm)
c
Microscope JEM-2100F
Accelerating Voltage 200 kV
Horizontal Field Width 2.4 um
500 nm
d
Microscope JEM-2100F
Accelerating Voltage 200 kV
Horizontal Field Width 37.9 nm
Magnification 600000 x
5 nm
e
Frequency
particle size (nm)

Figure 5

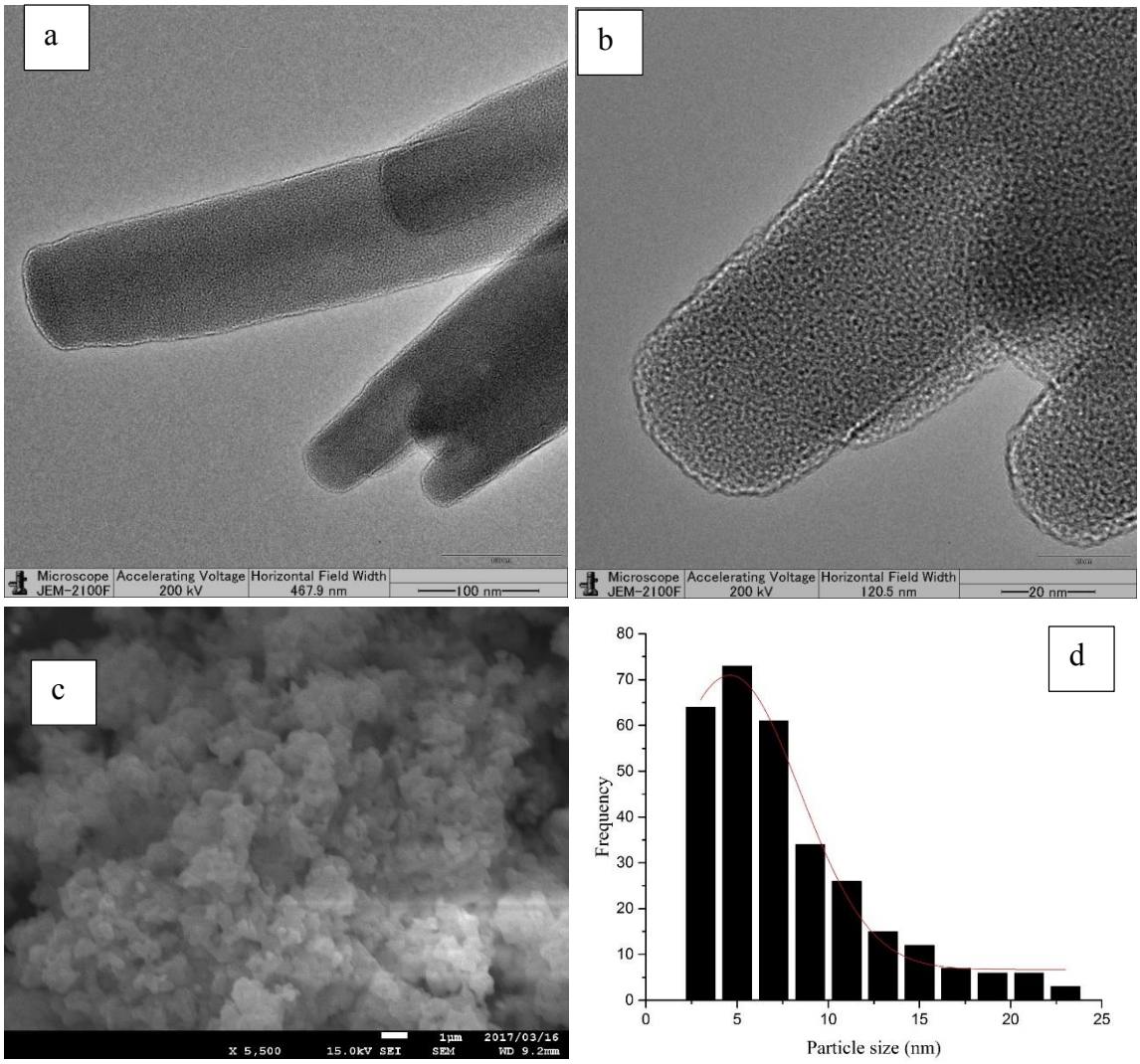
a
Microscope JEM-2100F
Accelerating Voltage 200 kV
Horizontal Field Width 467.9 nm
100 nm
b
Microscope JEM-2100F
Accelerating Voltage 200 kV
Horizontal Field Width 120.5 nm
20 nm
c
X 5,500 15.0kV SEI 1μm SEM 2017/03/16 WD 9.2mm
d
Frequency
Particle size (nm)
0
10
20
30
40
50
60
70
80
0
5
10
15
20
25

Figure 6

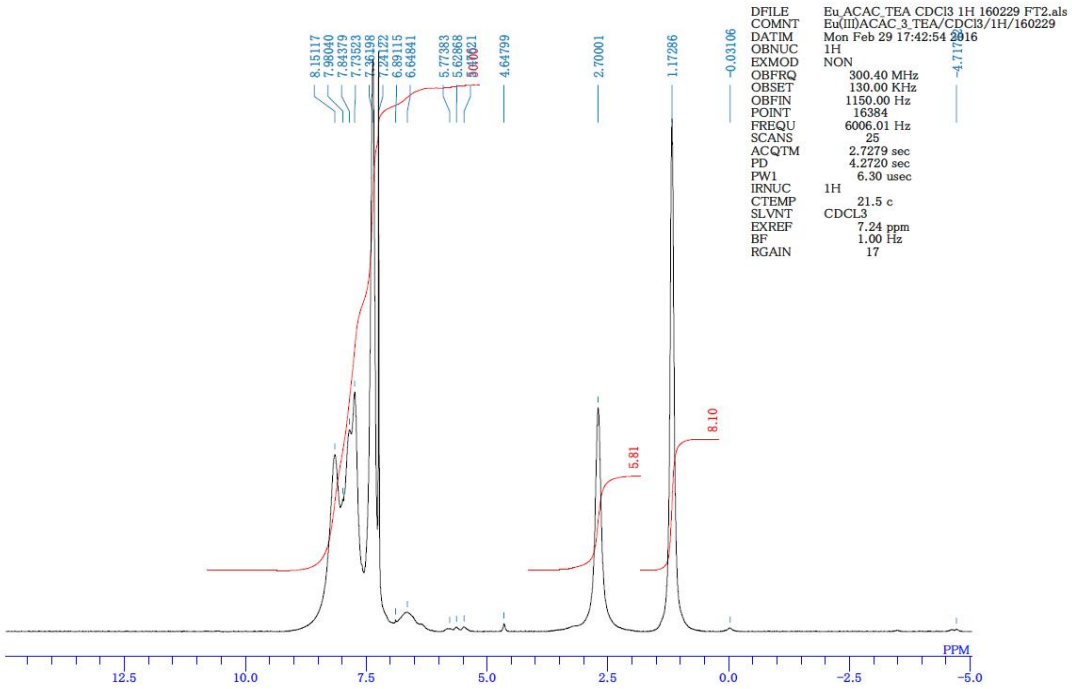
DFILE Eu_ACAC_TEA CDCl3 1H 160229 FT2.als
COMNT Eu(III)ACAC_3_TEA/CDCl3/1H/160229
DATIM Mon Feb 29 17:42:54 2016
OBNUC 1H
EXMOD NON
OBFRQ 300.40 MHz
OBSET 130.00 KHz
OBFIN 1150.00 Hz
POINT 16384
FREQU 6006.01 Hz
SCANS 25
ACQTM 2.7279 sec
PD 4.2720 sec
PW1 6.30 usec
IRNUC 1H
CTEMP 21.5 c
SLVNT CDCL3
EXREF 7.24 ppm
BF 1.00 Hz
RGAIN 17
8.15117
7.98040
7.89379
7.73523
7.36198
7.24122
6.89115
6.64841
5.77383
5.62868
4.64799
2.70001
1.17286
-0.03106
-4.17
5.81
8.10
PPM
12.5
10.0
7.5
5.0
2.5
0.0
-2.5
-5.0

Figure 7

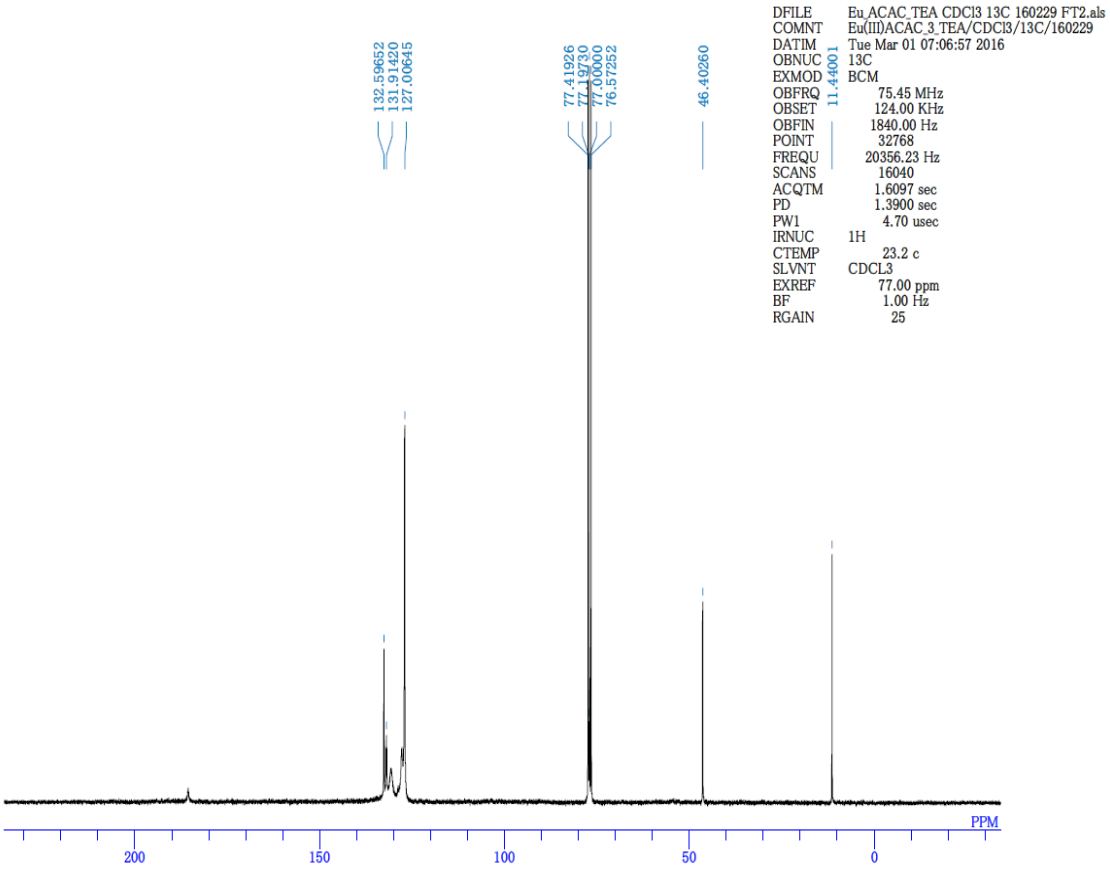
DFILE Eu_ACAC_TEA CDCl3 13C 160229 FT2.als
COMNT Eu(III)ACAC_3_TEA/CDCl3/13C/160229
DATIM Tue Mar 01 07:06:57 2016
OBNUC 13C
EXMOD BCM
OBFRQ 75.45 MHz
OBSET 124.00 KHz
OBFIN 1840.00 Hz
POINT 32768
FREQU 20356.23 Hz
SCANS 16040
ACQTM 1.6097 sec
PD 1.3900 sec
PW1 4.70 usec
IRNUC 1H
CTEMP 23.2 c
SLVNT CDCL3
EXREF 77.00 ppm
BF 1.00 Hz
RGAIN 25
132.59652
131.91420
127.00645
77.41926
77.19730
77.00000
76.57252
46.40260
11.44001
PPM
200
150
100
50
0

Figure 8

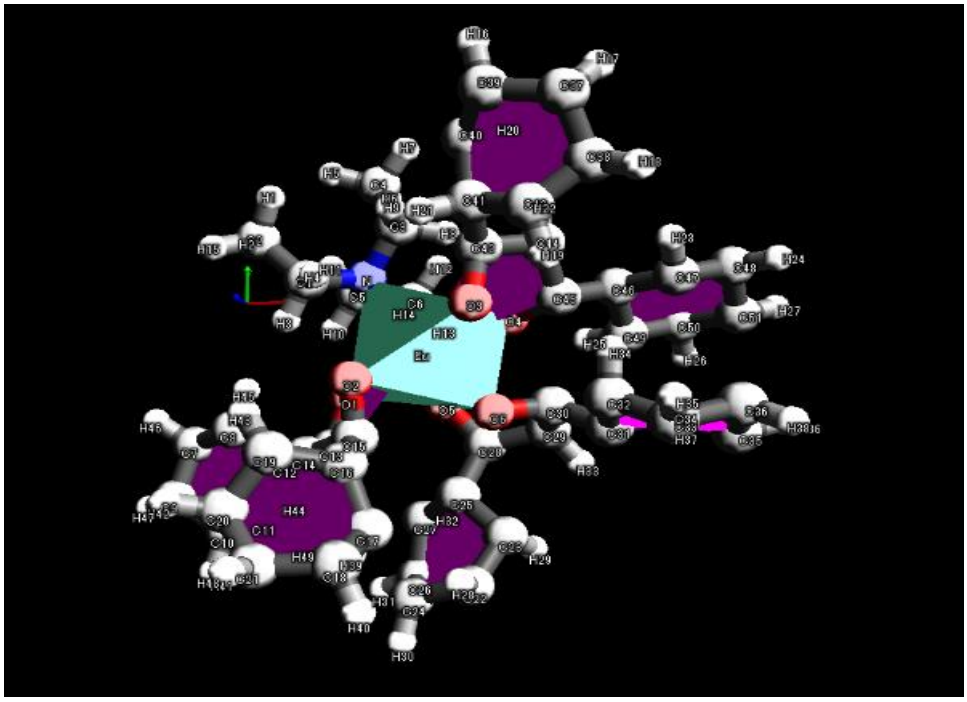

Figure 9

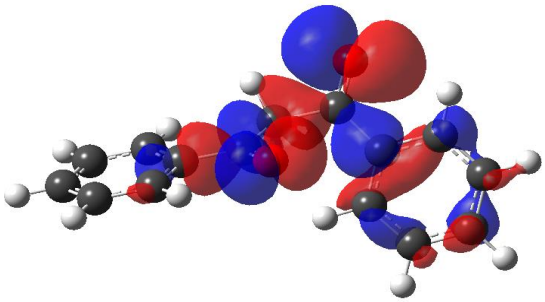

Dibenzoylmethane HOMO

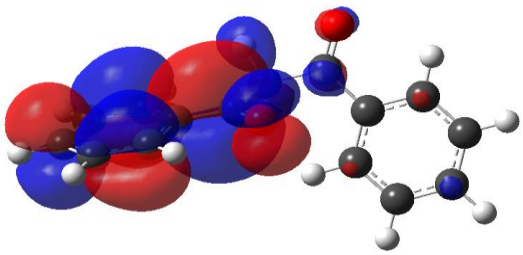

Dibenzoylmethane LUMO

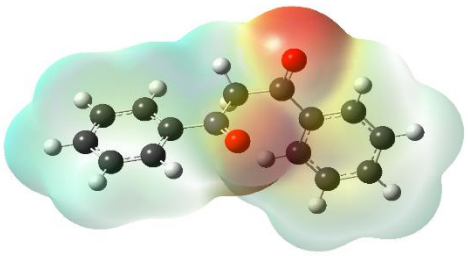

Dibenzoylmethane electron density mapping

Figure 10

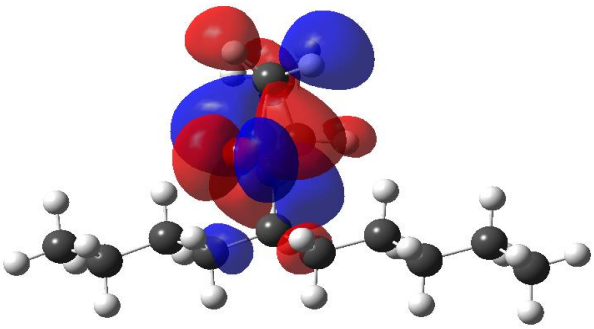

PVP LUMO 1

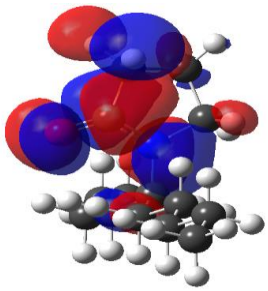

PVP LUMO 2

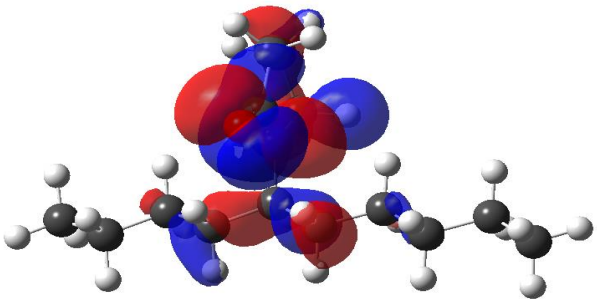

PVP HOMO 1

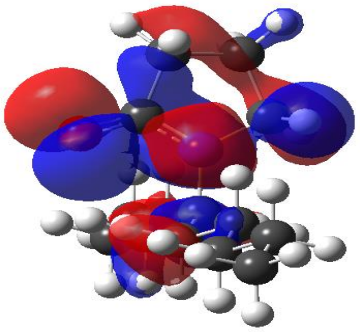

PVP HOMO 2

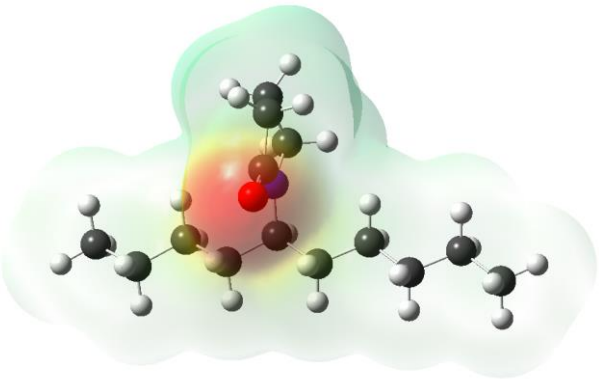

PVP electron density mapping

Figure 11

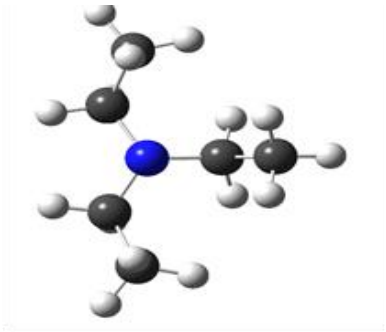

Triethylamine

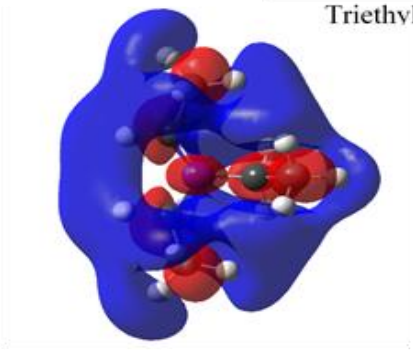

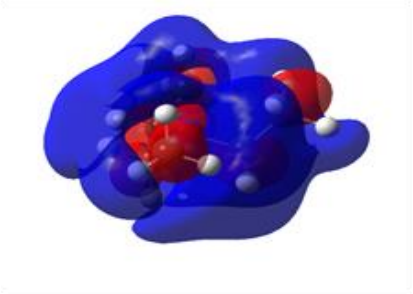

Triethylamine LUMO 1

Triethylamine LUMO2

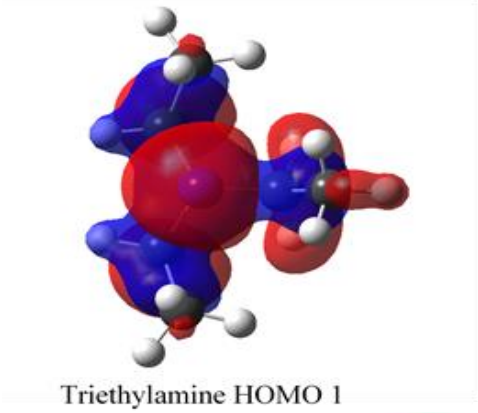

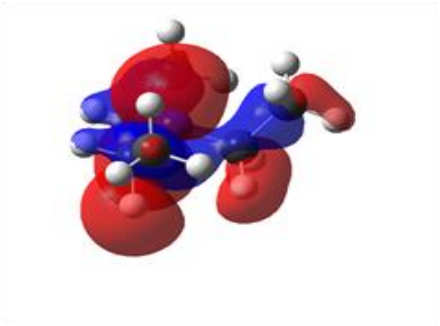

Triethylamine HOMO 1

Triethylamine HOMO 2

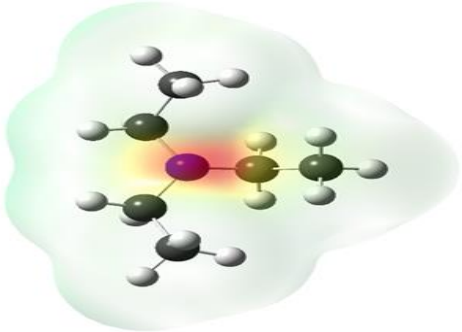

Triethylamine electron density mapping

Figure 12

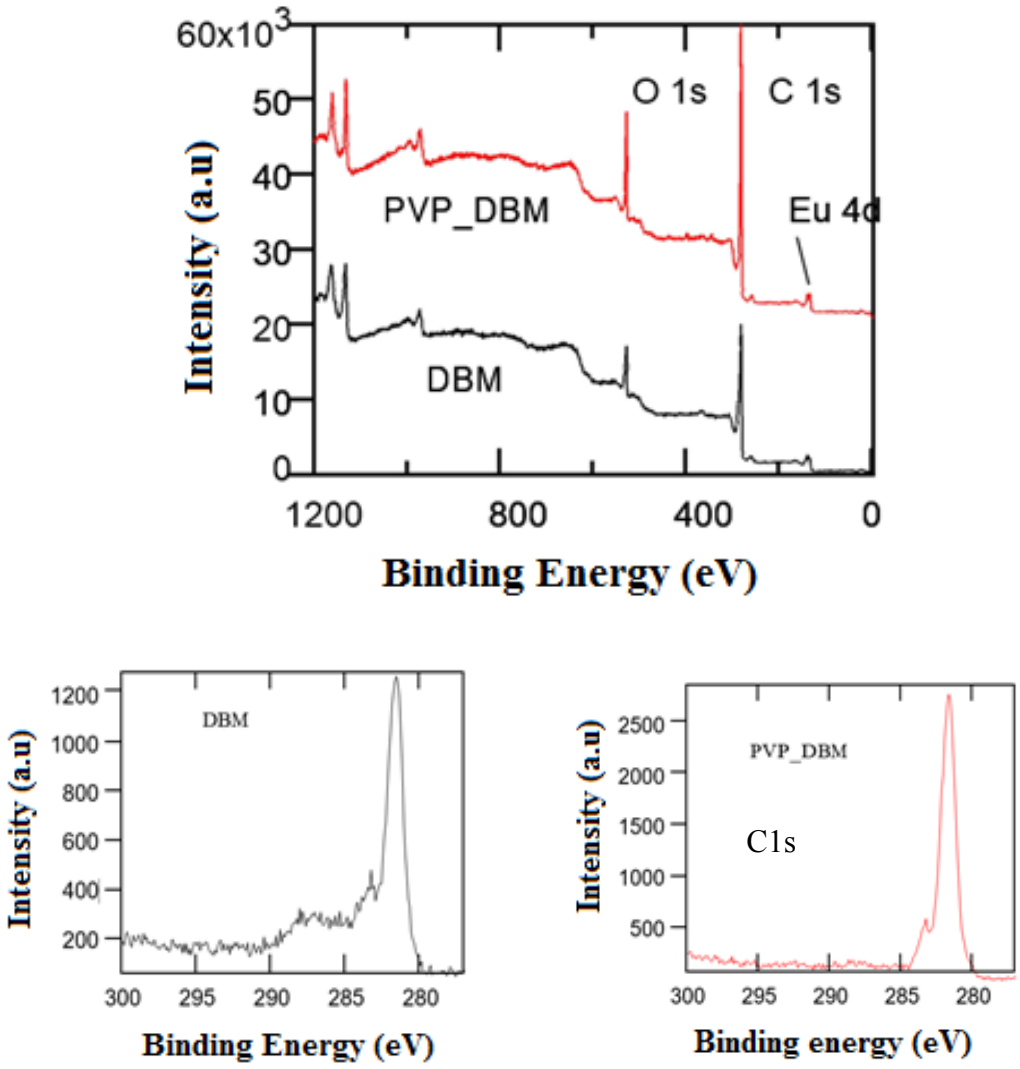
60x10^3
50
40
30
20
10
0
Intensity (a.u)
O 1s
C 1s
PVP_DBM
Eu 4d
DBM
1200
800
400
0
Binding Energy (eV)
1200
1000
800
600
400
200
DBM
Intensity (a.u)
300
295
290
285
280
Binding Energy (eV)
2500
2000
1500
1000
500
PVP_DBM
C1s
Intensity (a.u)
300
295
290
285
280
Binding energy (eV)

Figure 13

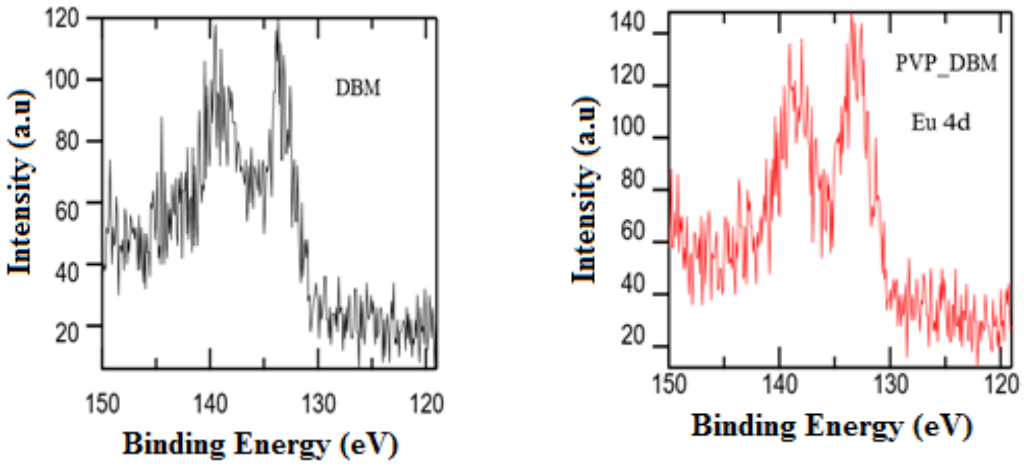

Figure 14

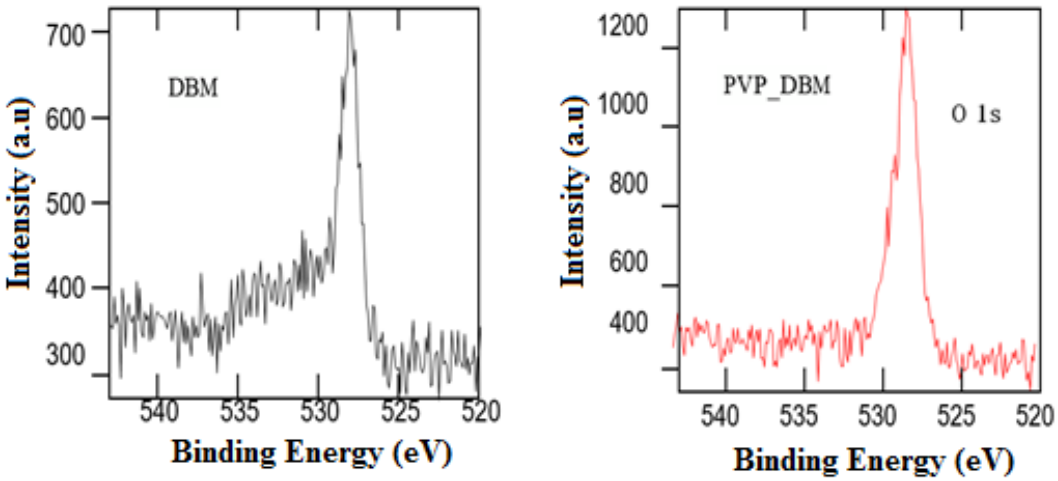

Figure 15